Final Technical Report

Funding Agency	Department of Energy
Document	Final Technical Report
Award Number	DE-EE0008980
Award Type	Cooperative Agreement
Prime Recipient	University of Central Florida Amber Thorne 407-823-3987 Amber.Thorne@ucf.edu
Prime Recipient Type	University
Project Title	Microdroplet Electrospray Localized Laser Printing and Sintering of Nanoparticles for Passivating, Carrier-Selective Contacts
Principal Investigator	Kristopher O. Davis, Ph.D. Assistant Professor Kristopher.Davis@ucf.edu
Final Report Authors	Jannatul F. Mousumi, Yahya Bougdid, Gunjan Kulkarni, Tianyi Li, Aravinda Kar, Ranganathan Kumar, Kristopher O. Davis
DUNS Number	150805653
Date of the Report	May 18, 2022
Project Period	February 1, 2020 to February 1, 2022

UCF College of Engineering and Computer Science

RISES

UCF CREOL, The College of Optics and Photonics

FSEC

Disclaimer

Executive Summary

In this project, the University of Central Florida (UCF) worked to develop a printing technology that could help address limitations of passivating, carrier-selective contact technologies for crystalline silicon (c-Si) photovoltaic (PV) cells. Traditionally c-Si PV cell architectures featuring homojunctions and metal contacts that directly come in contact with the c-Si absorber suffer from very high recombination at the metal/c-Si interface [1]–[10]. Passivating, carrier-selective contact are gaining traction in c-Si PV due to the lower recombination losses that can be achieved [11]–[15]. Currently, the two major passivating contact technologies are silicon heterojunctions (SHJ) and tunnel oxide passivating contacts (TOPCon). Both technologies are addressed in this project with processes developed for printing metal contacts SHJ solar cells and doped silicon lines using a microdroplet nanoparticle printing process combined with in-line laser sintering.

SHJ cells feature an amorphous silicon passivating contact that is not stable at high temperature and starts to degrade when annealed above 200°C [11]. Therefore, it requires low-temperature screen-printed silver (Ag) paste. The low temperature annealing yields Ag contacts with high bulk resistivity due to poor sintering and therefore requires higher Ag content in the paste, leading to higher production costs. With the improvement of the composition of the Ag paste for SHJ solar cells, bulk resistivitycan be reduced from 18 μΩ·cm to 5.5 μΩ·cm [16].

In this work, Ag inks and pastes were dispensed through a needle and then sintered with focused 10.6 μm continuous CO_2 laser energy to print the contact with low bulk resistivity and without any damage to the underneath amorphous silicon passivating layer. Unlike other metallization techniques, this process excludes the need for drying and annealing after printing the contact. The Ag ink/paste viscosity, needle diameter, substrate velocity, and flow rate were varied and the subsequent metal lines characterized in great detail to identify the optimal process conditions. Additionally, bulk resistivity values as low as ~7 μΩ·cm were achieved, nearly meeting the final project goal. The bulk resistivity can be further lowered down by using higher laser power/lower scanning speed. Contact resistivity values ranging from 23.4-42.2 $m\Omega \cdot cm^2$ were realized on the textured SHJ samples without any passivation damage using this printing process.

Another excellent and currently industrially relevant passivating carrier selective contact technology is silicon oxide (SiO_x) passivated doped polycrystalline silicon (poly-Si) contact. This contact technology consists of an ultrathin 1-2 nm of SiO_x layer and a doped poly-Si layer and provides excellent surface passivation quality and has been incorporated into PV cells featuring conversion efficiencies of more than 26% [13]. In this work, this contact was formed using a SiO_x layer grown by deionized water with ozone (DI-O_3) and *in situ* phosphorus-doped poly-Si layer deposited using atmospheric pressure chemical vapor deposition (APCVD) process. APCVD is more simple, cost effective, and suitable for an industrial production line compared to PECVD and LPCVD as this is an in-line process and does not require any vacuum/plasma systems. Additionally, the influence of different process parameters on the passivation quality and carrier selectivity has been studied. After hydrogenation saturation current density (J_0) less than 5 fA/cm^2 has been achieved using which indicates excellent surface passivation quality of the APCVD doped poly-Si passivating contact.

However, the heavily doped poly-Si contact causes optical losses due to parasitic absorption when used as the front contact. Though thinning down the doped poly-Si region in the unmetallized region improves the efficiency by decreasing the absorption losses, it leads to metallization induced passivation damage. In this work, a system is developed to print narrow doped poly-Si lines so that there will be thick doped poly-Si layers only under metallized region. The silicon lines has been printed by sintering arsenic doped silicon nanoparticles ink using 1064 nm Nd:YAG laser. The influence of the laser power power on the quality of the printed silicon line and on the passivation quality of the poly-Si contact layer has been studied.

The following accomplishments have been made on this project.

- The team demonstrated a novel metal contact printing system for SHJ solar cells where Ag nanoparticle-based inks and pastes are sintered using laser energy and printed onto the SHJ substrates.
- Ag line widths as low as 110 μm and average line heights around 20 μm have been achieved using single pass Ag printing with this printing process.
- Bulk resistivity values as low as 7 μΩ·cm has been realized for these laser sintered Ag contacts.
- Contact resistivity values ranging from ~23.4 $m\Omega \cdot cm^2$ to ~ 42.2 $m\Omega \cdot cm^2$ have been achieved on these contacts.
- Cross-sectional SEM imaging was performed to investigate the interface and the sintering quality of the metal contact. EDS analysis on the printed contact showed the deposition of Ag without significant amounts of carbon and oxygen present in the metal line.
- A spatially-resolved optical and thermal model for the Ag laser sintering has been developed and validated, thus enabling predictive calculations of the optimum laser processing parameters [17].
- High quality passivating electron contacts have been fabricated using DI-O_3 SiO_x passivation with an APCVD P-doped poly-Si film [18]. The influence of the deposition temperature, gas ratio, and annealing temperature on the structure, properties, and performance of the passivating contacts has been investigated thoroughly. The optimal annealing temperature and time for developing the passivating contacts (i.e., 850°C for 30 minutes) has been determined. Saturation current densities values as low as 3 fA/cm^2 have been achieved for the optimized contact.
- The team printed doped poly-Si lines on the SiO_x based APCVD phosphorus doped poly-Si passivated Si substrates using 1064 nm Nd:YAG laser sintering of the arsenic doped Si nanoparticles ink. Influence of the laser power has been investigated on the line width, line quality, and the laser induced passivation damage.
- The team published two peer-reviewed journal articles [17], [18], with another one in the process of being finalized for submission. Two conference proceedings papers were also published at the *IEEE Photovoltaic Specialists Conference*.

Table of Contents

1. Introduction

In this project, the team used a nanoparticle electrospray laser deposition (NELD) process developed at the University of Central Florida (UCF) to address current limitations of passivating, carrier-selective contact technologies for crystalline silicon (c-Si) photovoltaic (PV) cells. The NELD process was used to print low bulk line resistivity (ρ_b) Ag contacts directly onto transparent conductive oxides (TCOs), like indium tin oxide (ITO), for hydrogenated amorphous silicon (a-Si:H) based c-Si heterojunction (SHJ) cells without any subsequent contact firing step needed (Figure 1a). One glaring limitation of a-Si:H SHJ cells is the high cost and high bulk line resistivity of the low temperature Ag pastes used in these cells. Low temperature pastes are more expensive per kg, and as much as double the amount of Ag is required when compared to the higher temperature Ag pastes used for Al-BSF and PERC cells [19]. These pastes are required because the passivation at the a-Si:H(i)/c-Si interface will degrade if annealed above 200°C [11], and this temperature limit results in poor sintering of the Ag contacts. This issue also applies to transition metal oxide (TMO) heterojunctions, which also have comparable temperature limitations [20]–[28]. Increasing ρ_b in a manner that doesn't impact the passivation of the a-Si:H(*i*)/c-Si interface can yield obvious efficiency improvements due to reduced metal coverage and cost reductions due to less Ag usage and the higher maximum power (P_{MP}) obtained for each cell.

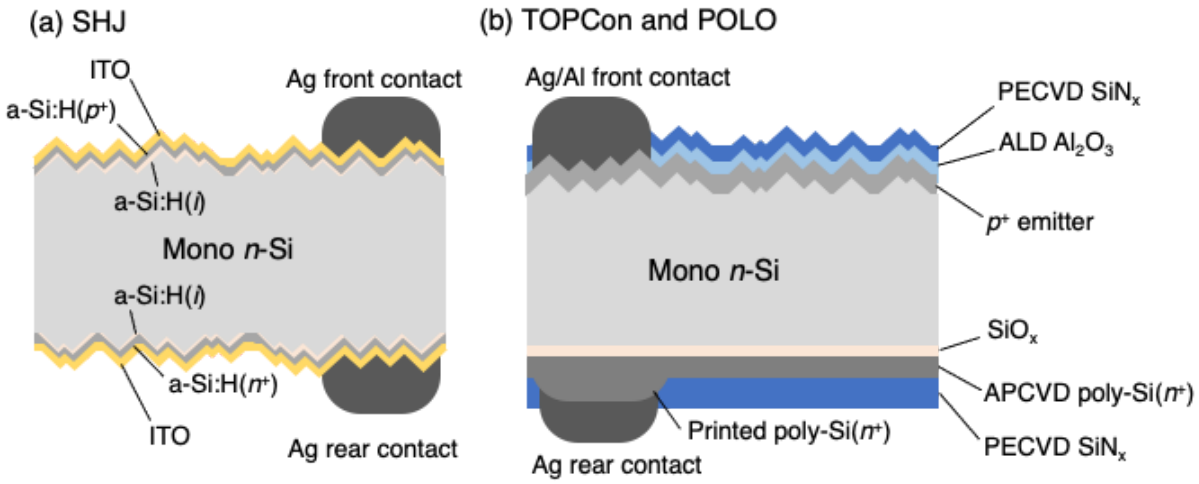

Figure 1. (a) Schematic of a SHJ cell featuring the printed Ag contacts. (b) Schematic of a *n*-type TOPCon or POLO cell featuring the localized poly-Si contact printed on top of a thin poly-Si film, deposited by APCVD in this project. The role of the printed layer is to locally thicken the poly-Si underneath the metallization to limit metal-induced recombination, a known issue for TOPCon and POLO cells featuring fire-through metal contacts on the rear.

In addition to SHJ cells, this project also targeted improvements to another passivating, carrier-selective contact technology - tunnel oxide passivating contacts (TOPCon) and polycrystalline on oxide (POLO). TOPCon and POLO cells use very thin silicon oxide (SiO_x) passivation films coupled with a heavily doped poly-Si film and have emerged as an excellent approach to forming passivating, carrier-selective contacts [29]. The following characteristics enable these contacts to simultaneously achieve a

low contact recombination (J_{0C}) and contact resistivity (ρ_c): the passivation of dangling bonds by the SiO_x layer; favorable band-bending at the interface to restrict minority carrier flow; and either quantum mechanical tunneling through the thin SiO_x layer or direct conduction through pinholes formed in the oxide[30]–[35]. Cell efficiency as high as 26.1% has been reported using the contact in interdigitated back contact (IBC) cells [36], [37]. Unlike a-Si:H-based SHJ cells, poly-Si passivating contacts can tolerate higher temperature, making them compatible with high temperature metallization processes [38].

Low pressure chemical vapor deposition process (LPCVD) [37], [39], [40] and plasma enhanced chemical vapor deposition (PECVD) [41]–[43] have been the primary deposition technologies used to date to deposit the thin silicon films, but physical vapor deposition (PVD) [44] has also been used. The as-deposited silicon layers go through a high temperature post-deposition process for solid phase crystallization of the silicon layer, as well as either doping with phosphorus or boron in the case of ex situ doping or dopant activation in the case of in situ doping. However, all of these deposition techniques require vacuum systems and/or a plasma source, adding complexity and cost to the manufacturing process.

In this project, the team used in-line atmospheric pressure chemical vapor deposition (APCVD) as a simpler and more cost-effective deposition process compared to the above-mentioned processes (LPCVD, PECVD, and PVD). This process requires no vacuum or plasma systems and is a single-side deposition process, making it highly suitable for high-volume PV cell manufacturing. A new approach of printing localized poly-Si lines directly onto the SiO_x-passivated APCVD poly-Si contact was explored (Figure 1b). In most applications, the doped poly-Si contacts are placed at the back side of PV cells [42], [45], [46] because the use of a poly-Si film on the front would lead to high parasitic optical absorption [47]. Previous studies show that short-circuit current density values (J_{SC}) in the range of 0.4-1 mA/cm^2 are lost for every 10 nm of poly-Si material [48], [49]. The optical loss due to the absorption in the doped poly-Si can be reduced by thinning down the poly-Si layer, but this can lead to metal-induced recombination if the metal punches through the thin poly-Si film. Adding another layer of doped poly-Si only under the metallized region can resolve this issue. This benefits the contact structure in two ways: (i) less optical loss because of the thin layer of poly-Si in non-metallized region of front contact; and (ii) no/very low passivation damage from the metallization as the extra layer of poly-Si protects the thin APCVD poly-Si layer underneath. Keeping the CVD poly-Si film is also important, because the processing cost scales directly with film thickness [50]. In this work, a novel laser assisted sintering and printing system is presented to print a thin and a narrow layer of doped poly-Si layer. In this process, doped silicon nanoparticle ink is dispensed through a needle with a very small diameter and the nanoparticles are sintered using a laser energy to print a narrow doped poly-Si line on the APCVD doped poly-Si contact.

2. Project Experimental Methods

2.1 Silver Printing

Figure 2 highlights the laser-substrate interaction and the Ag nanoflake dispenser for Ag line deposition on ITO-coated Si substrate using the NELD process. A paste of Ag nanoflakes is delivered to the laser-substrate interaction zone using a capillary tube of inner diameter (ID) of 108 μm (Figure 2a). Figure 2b shows an ITO-coated Si substrate on a linear stage, and a syringe pump that pushes the plunger in a syringe (Figure 2c) for delivering the paste onto the substrate. The paste interacts with a continuous wave CO_2 laser of wavelength 10.6 μm.

The original Gaussian beam coming from a CO_2 laser source is converted into an annular beam of nearly uniform radial irradiance distribution using axicon and biconvex lenses, and the annular beam is focused with a parabolic mirror to form a hollow laser cone (Figure 2a,b). At the focal point of the parabolic mirror, i.e., at the apex of the cone, the original Gaussian beam transforms to a Gauss-Bessel beam with an irradiance distribution different from the typical Gaussian irradiance distribution. The interaction among the laser, paste and substrate occurs at the apex of this cone, and the interaction process is controlled to deposit Ag lines in two steps, drying of the paste and sintering of the nanoflakes. The paste is heated with a low laser power (2.3W) to evaporate the liquid of the paste during the drying process and then the laser power is increased to 11.8 W to accomplish sintering of the nanoflakes and adherence of the Ag line to the substrate. The substrate is moved beneath the laser beam by operating the linear stage at the speed of 1 mm/sec for both the drying and sintering steps. Also the diameter of the laser beam on the substrate surface is set at 300 μm for both steps.

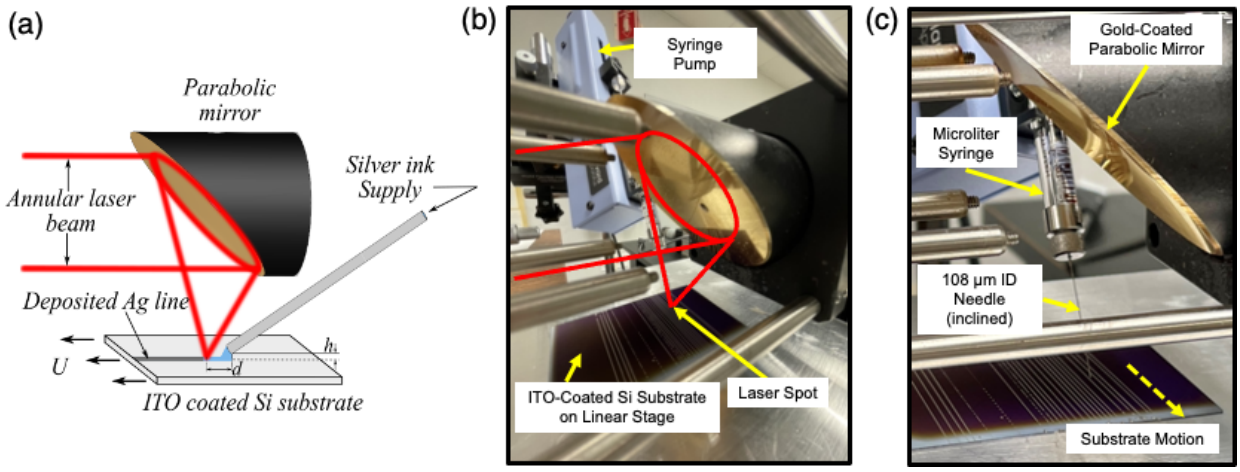

Figure 2. (a) Illustration of the experimental setup used to print and sinter Ag contacts. (b) Picture of the actual setup. (c) Zoomed in view of how the Ag paste is delivered.

2.2 APCVD Poly-Si Thin Film Deposition

Symmetrical test structures consisted of poly-Si/SiO_x/c-Si/SiO_x/poly-Si were fabricated using quartered 156 mm *n*-type Czochralski (Cz) wafers with a {100} surface, base resistivity of 1-3 Ω·cm, and wafer thickness of approximately 200 μm. The wafers were first passivated with a ~1.5 nm SiO_x layer grown using DI ozonated water. An *in situ* phosphorus doped thin silicon layer was deposited on the oxide coated substrates via

APCVD (Figure 3), a process previously known for depositing various oxides for c-Si PV cells [51]–[56]. The phosphorus doped silicon layer was deposited from the thermal dissociation of silane (SiH_4) and phosphine (PH_3) gases. Different deposition zone temperatures (695°C and 750°C) and PH_3 gas ratio were used during the deposition (Table 1). The as-deposited samples were annealed at high temperature for the passivation activation of the contacts.

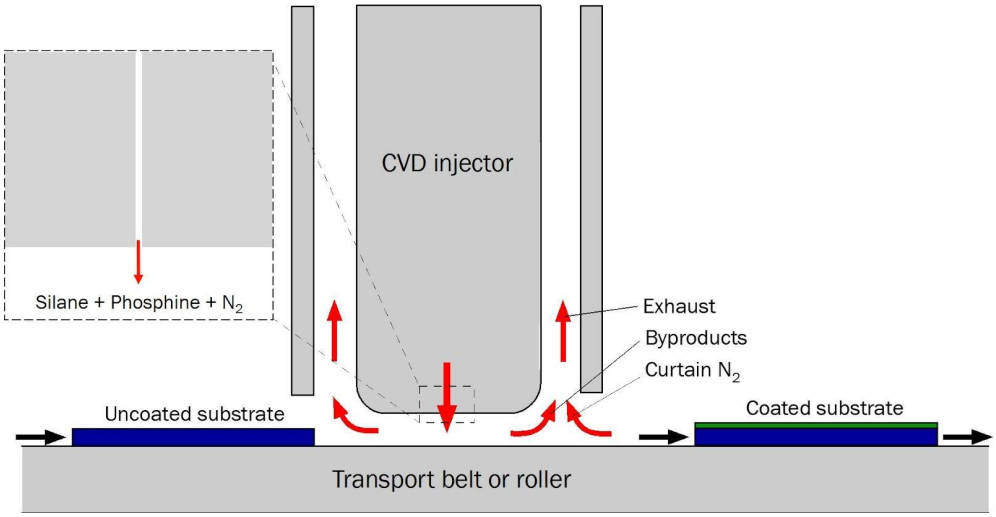

Figure 3. Illustration of the APCVD system used to form the passivating poly-Si electron contacts for subsequent printing.

Table 1. Deposition temperatures and gas ratio for the phosphorus doped silicon deposition.

Batch	Deposition zone temperature (°C)	PH_3 ratio (%)
275	695	1.48
276	695	4.00
277	695	9.09
280	750	1.48
281	750	4.00
282	750	9.09

2.3 Poly-Si Printing

For the Si line printing, the substrates featuring the APCVD poly-Si films described above were used for printing (phosphorus-doped, 100 nm thick poly-Si, then SiO_x, less than 2 nm, then c-Si, 200 µm thick). The nanoparticle suspension consisted of n^{++} degenerately arsenic-doped Si nanoparticles (~80-100 nm) dispersed in ethylene glycol with 75 wt% Si. Prior to deposition, approximately 7 mL of this suspension was ultrasonicated for 30 minutes at 80 MHz frequency, and the resulting suspension was

used to deposit Si lines on APCVD poly-Si substrates using the NELD process. The substrate was placed on a linear stage to move it continuously at a specific speed for depositing continuous and homogenous Si lines at desired locations on the poly-Si substrate.

The experimental set up is similar to the one used for Ag line deposition except that a pulsed Nd:YAG laser of wavelength 104 nm was employed for drying (pre-heating) and sintering the Si nanoparticles because of the difference in the optical properties of Ag and Si. The Ag paste was found to absorb the CO_2 laser better, while the n^{++} Si nanoparticle suspension is relatively transparent to the long 10.6 μm wavelength. The Nd:YAG laser was therefore better suited for sintering of the nanoparticles. For both cases of Ag and Si line deposition, however, the original Gaussian beam of the laser source was transformed to an annular beam using axicon and biconvex lenses and subsequently modified to a Gauss-Bessel beam using a parabolic mirror (Figure 4). The laser system was operated at the pulse repetition rate of 30 kHz and pulse length of 170 ns, the average power of the laser used for sintering was fixed at 13 W, and the diameter of the laser beam on the substrate surface was ~500 μm. For the drying step, however, the average power was chosen to be 3 W. The substrate was moved at a speed of 1 mm/s for both the drying and sintering steps. The sintered samples were cleaned in an ultrasonic bath which was operated at 20 kHz for 10 min. This procedure yields clean samples by removing the excess Si nanoparticles that are not completely sintered.

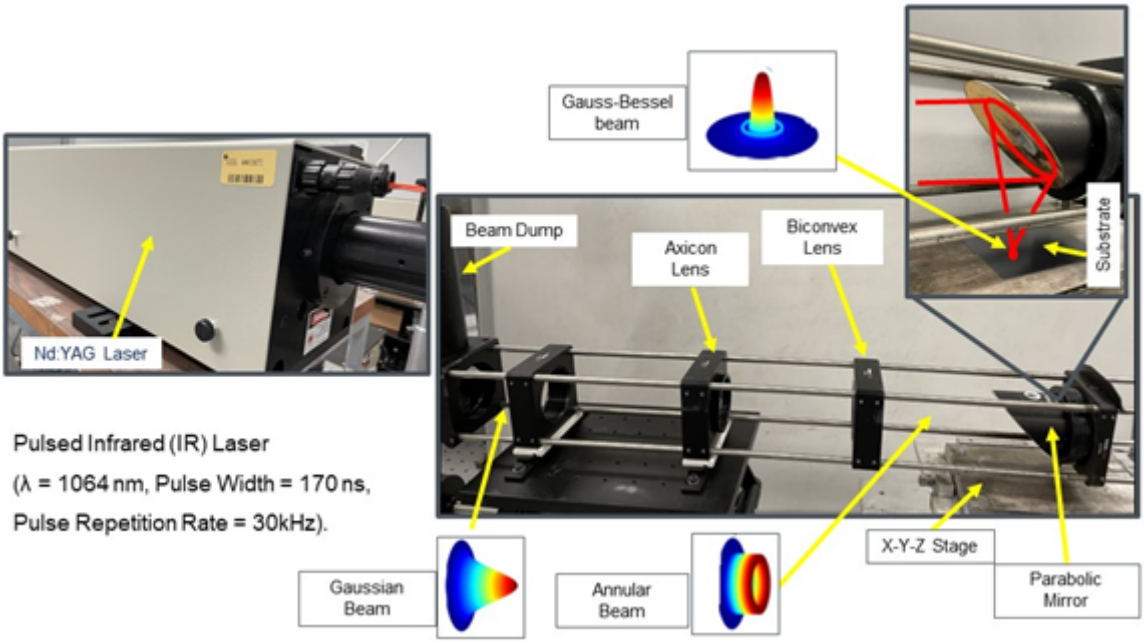

Figure 4. Experimental setup used to print the doped Si nanoparticles. (Left) Pulsed Nd:YAG Laser system (λ = 1064 nm). (Right) Optical system utilized for pre-heating and laser sintering of Si nanoparticles.

2.4 Electrical Characterization

Two of the most important figures of merit in this project are the bulk resistivity of the printed Ag fingers (i.e., ρ_b) and interfacial contact resistivity between the Ag finger and the underlying ITO (i.e., ρ_c). The ρ_b is a bulk material property of the printed Ag that can

be determined with the equation below by measuring the resistance of the printed Ag lines and their geometry (Figure 5).

$$R\ (\Omega) = \rho_b\ (\Omega \cdot cm)\ \frac{L\ (cm)}{A\ (cm^2)}$$

Here, *L* is the length of the Ag finger, *A* is the cross-sectional area of the Ag finger, and *R* is the resistance of the Ag finger.

The cross-sectional area is considered rectangular for the Ag lines with very small height (≤ 2 μm). For this case *A* is calculated using the equation below:

$$A = w \times t$$

From the profilometer and SEM images of the lines printed with Ag paste, a gaussian shaped cross-sectional area is observed (Figure 5b).

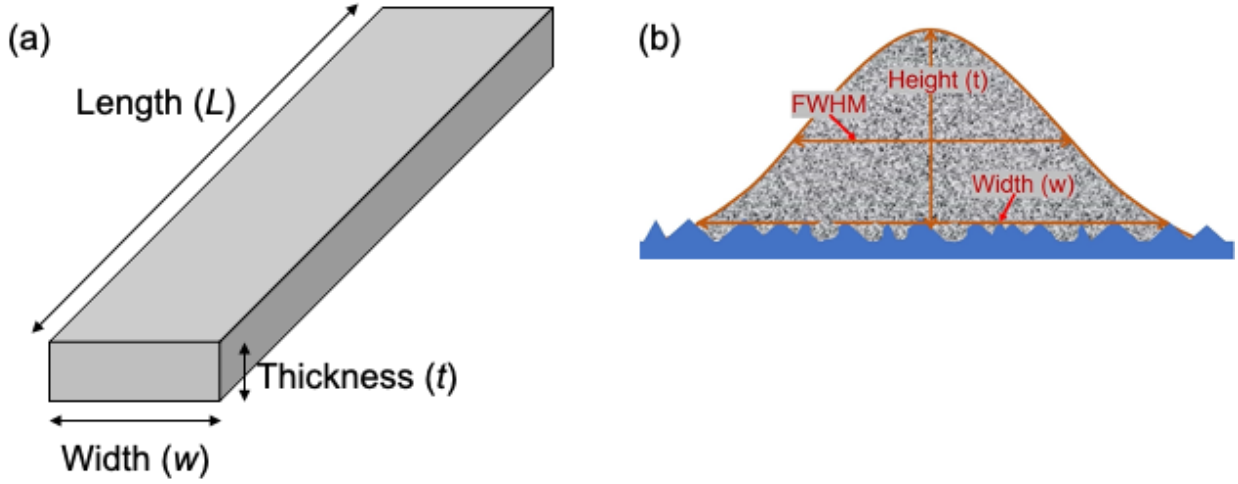

Figure 5. Geometry of the printed Ag lines used to determine ρ_b (a) for Ag lines with very small height and rectangular shaped cross-sectional area deposited using Ag ink and (b) for Ag lines with gaussian shaped cross sectional area deposited using Ag paste. Figure taken from [6].

In such cases, A is calculated using following equation [57]:

$$A = \frac{s \times w \times t \times \sqrt{\pi}}{2 \times \sqrt{ln2}}$$

where *s* = FWHM/*w* and FWHM indicates full width half maximum of the Ag line.

Four-wire current-voltage (I-V) measurements (i.e., Kelvin measurements) were performed on the printed Ag fingers using a ContactSpot (Figure 6 left) to measure the total resistance. Additionally, a Jandel four-point probe system (Figure 6 right) was used to measure the sheet resistance (R_{sheet}) of the ITO films, as well as the R_{sheet} of the

doped poly-Si films. Measurements of ρ_c are also being performed with the ContactSpot system using best practices developed by the UCF team over the past few years [58]–[60].

The length of the printed Ag fingers is at least 2.5-3 cm in all cases and is easy to measure. The cross-sectional area of the Ag fingers is highly dependent on the rheological properties of the nanosuspensions used and the process parameters. The width of the Ag fingers can be measured with an optical microscope, but the thickness is a bit more challenging. It is possible to measure this with a profilometer on planar surfaces, but this is more challenging to do on textured surfaces. For this reason, a Hitachi TM3000 SEM was used to determine the thickness. This was accomplished by laser scribing and cleaving the samples and acquiring a SEM image of the exposed cross-section.

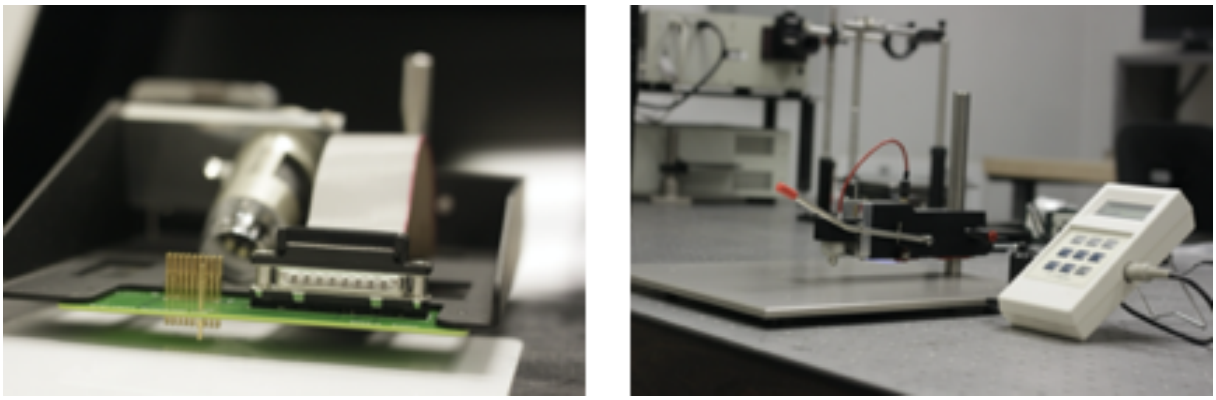

Figure 6. (Left) *ContactSpot* system manufactured by BrightSpot Automation. (Right) Four-point probe system made by Jandel.

2.5 Optoelectronic Characterization

While lowering the series resistance losses of a-Si:H/c-Si SHJ cells is important, it cannot come at the expense of increasing charge carrier recombination since this is the main advantage of these types of cells. To detect and quantify any potential increases (or decreases) in recombination following Ag printing and laser sintering, a number of different optoelectronic characterization methods were used in this project. Before printing, photoconductance-calibrated photoluminescence (PL) imaging was performed to create images of the excess carrier concentration (Δn), the effective carrier lifetime (τ_{eff}), and the implied open-circuit voltage (iV_{OC}) using a LIS-R1 system made by BT Imaging (Figure 7). PL images were also taken after metallization, and any changes in the PL image near the contacts can be related directly to changes in Δn and iV_{OC}. For samples featuring a full double heterostructure, Suns-V_{OC} measurements are also performed after metallization. Monitoring changes in the Suns-V_{OC} of these structures has proven to be very effective in experiments aimed at determining what optical power and energy the Ag contacts can handle before a loss in V_{OC} is observed.

The methods above are also being applied to doped poly-Si samples, albeit not on cells, but primarily on symmetrical test structures. For these samples, we really need to accurately determine the saturation current density (J_0) of this passivating contact without the influence of other sources of recombination.

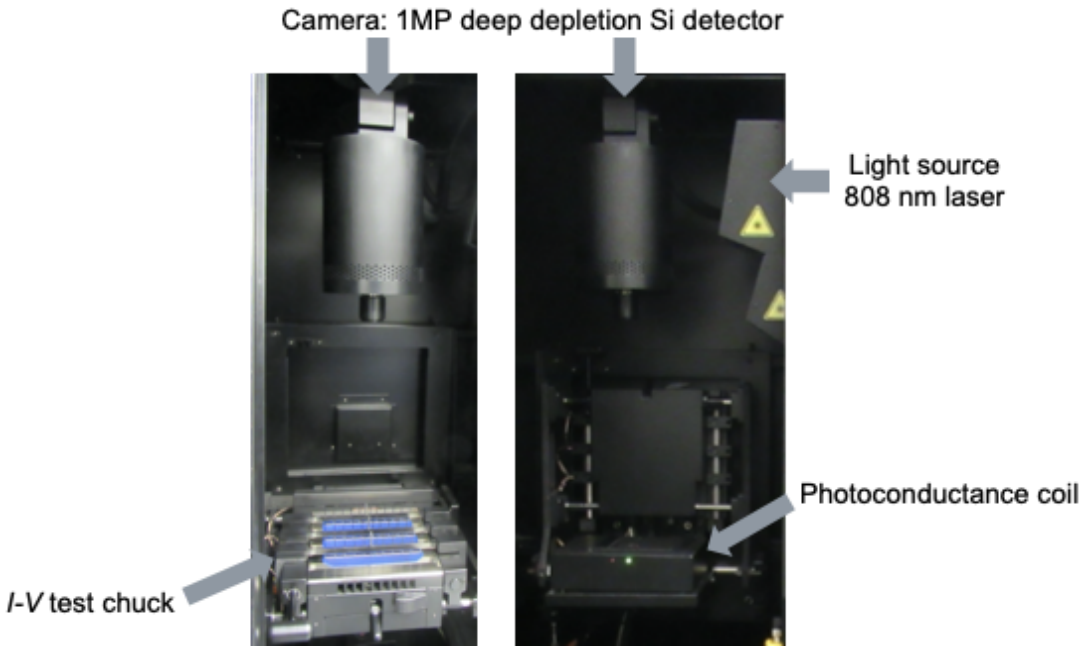

Figure 7. BT Imaging LIS-R1 system used for PL imaging. (Left) Configured with an *I-V* test chuck for measurements on metallized PV cells. (Right) Configured with a photoconductance coil for measurements on unmetallized wafers.

2.6 Materials Characterization

Materials characterization is very important to optimize any system, process, and products as it helps us to understand the relationships between process, structure, properties, and performance. In this project, different materials characterization methods were used in the development of the laser sintered Ag contacts, APCVD doped poly-Si contacts, and laser sintered doped poly-Si lines.

Top-down and cross sectional scanning electron microscopy (SEM) imaging were performed to investigate the microstructure, sintering quality, and the interface with the substrate of the laser printed Ag contacts. Energy dispersive X-ray spectroscopy (EDS) was performed for the elemental analysis of the Ag lines. ZEISS SmartSEM software was used to collect and analyze the images and the EDS data. For SEM imaging and EDS analysis two systems were used. One was a Hitachi High-Tech TM3000 TableTop SEM and another one was a ZEISS ULTRA 55 SEM system. For Hitachi TableTop SEM an acceleration voltage of 15 kV and working distance of around 6 mm were used for the imaging. And for ZEISS ULTRA 55 SEM system, an acceleration voltage of 3 kV and working distance less than 3 mm were used to capture the images. EDS analysis in ZEISS ULTRA 55 SEM system was performed using 25 kV acceleration voltage, working distance of 13 mm, and the EDS detector. For the cross-sectional imaging of the laser printed contact, the samples were scribed with laser at the back-side and then cleaved. To investigate the interface of the Ag contact with textured surface, the surface of the laser cut and cleaved samples were cleaned with focused ion beam (FIB) using a FEI Helios 460F1 system.

The passivation quality and carrier selectivity of the doped poly-Si contacts largely depend on the dopant and hydrogen concentration of the films and at/near interfaces. To investigate the influence of the factors, secondary ion mass spectrometry (SIMS)

was performed using a PHI Adept 1010 Dynamic SIMS system. Cesium (Cs) ion beam with 3 kV energy as the primary beam with 300 μm raster size, 5% detection area, and 40-50 nA beam current.

Crystallinity of the doped poly-Si films was investigated by performing grazing incidence X-ray diffraction (GI-XRD) and Raman spectroscopy. The XRD spectra were obtained using Cu-Kα radiation with a wavelength of 1.54 Å at a fixed incidence angle of ω = 5°. The incidence angle was kept low enough so that all the data were collected only from the APCVD Si films. And Raman spectroscopy was performed on a Horiba® LabRam HR Evolution system with a 473 nm excitation wavelength. This blue laser allows for a short penetration depth. A 100× objective, 1800 gratings/mm and 10% neutral density filter were used for the single point scans. A laser intensity of 1.9 mW with spot diameter of 641 nm was used for the scans. The experimental conditions were 5 second integration time and 5 accumulations. Prior to conducting any Raman measurements, the equipment was calibrated using a standard calibration objective. Surface topography of the APCVD Si layers was characterized using atomic force microscopy (AFM). To prepare the samples for AFM measurements, APCVD Si films were deposited on mirror polished Si wafer. AFM scans were performed in tapping mode using the Veeco/DI Dimension 3100 AFM system over 1 μm^2 surface area.

3. Project Results and Discussion

3.1 Printed Silver Contacts on ITO Thin Films for a-Si:H/c-Si SHJ Cells

3.1.1 Experimental Progress Over Time

Figure 8 below shows a summary of the team's progress to date on this project. In Figure 8a, the line resistance, line width, and line height of printed Ag contacts are shown versus run number. You will notice there is a sharp increase in the line height and because of this, a strong and repeatable drop in the line resistance in the most recent data. This was achieved due to a new Ag paste, equipment improvements, and process optimization. The ability to print tall Ag contacts and still get uniform sintering throughout the contact using the CO_2 laser were critical in achieving the low line resistance values. By the end of the project, narrow line widths and low line resistances were achieved, important steps in minimizing both the series resistance (R_S) losses and optical shading losses (Figure 8b). Ultimately, our team came very close to achieving the final project milestones for bulk resistivity and line width (Figure 8c).

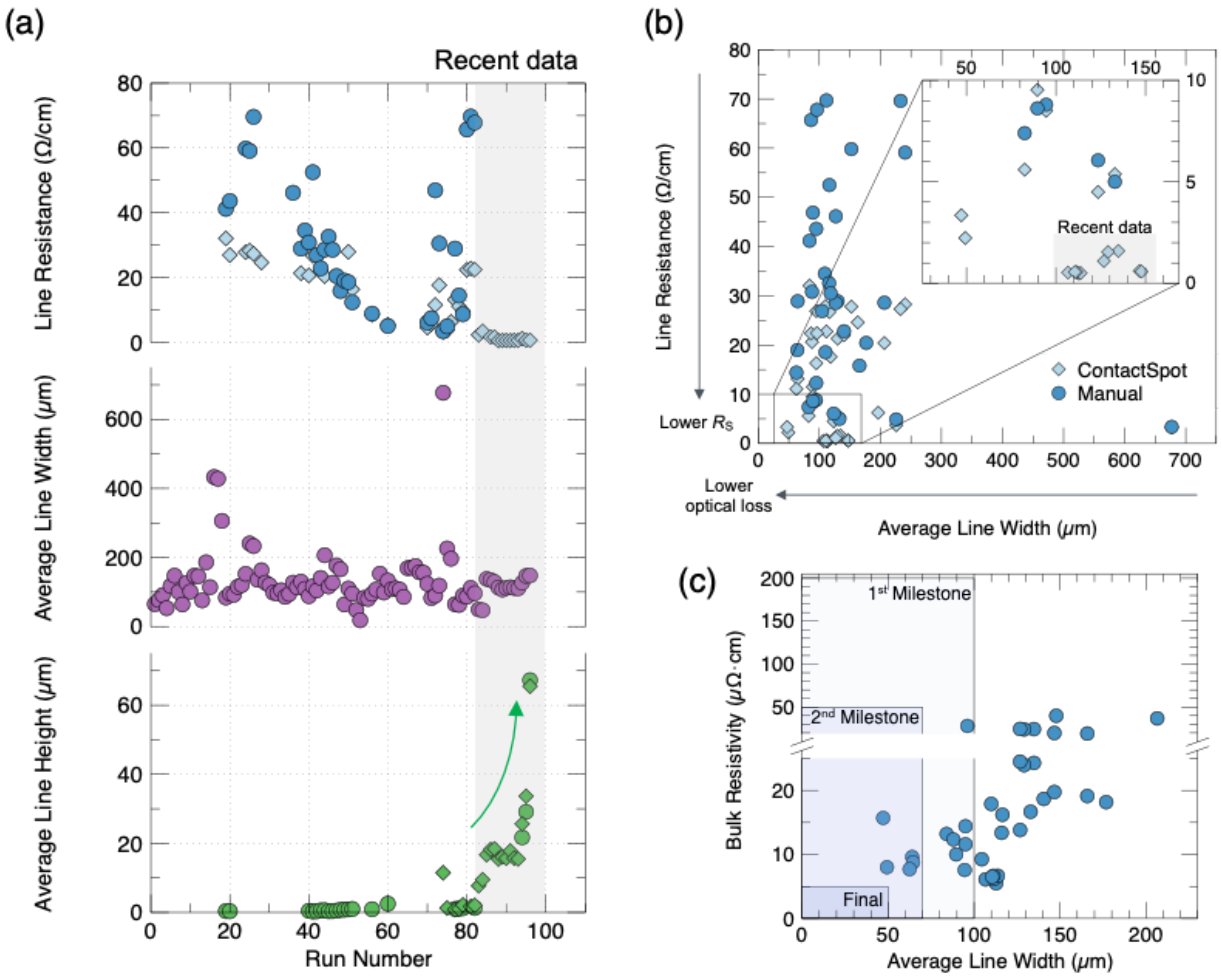

Figure 8. (a) The line resistance, average line width, and average line height of the printed Ag contacts over time throughout the course of this project. (b) Line resistance versus average line width for the printed Ag contacts with a magnified portion highlighting the lower left corner of the graph, the region with both the lowest R_S and optical losses. (c) Bulk resistivity versus average line width for the printed Ag contacts highlighting the project milestones.

3.1.2 Detailed Characterization of High Quality Silver Contacts

Some examples of the improved Ag contacts featuring an increased height and better line width repeatability are shown in Figure 9. The image in Figure 9a shows continuous and uniform line widths. The optical microscopy images (Figure 9b) also show this uniformity under magnification. In addition to achieving low line resistance, we have also shown the contacts have a low contact resistivity very close to the final project goal (Figure 9c). Table 2 lists the average line width, height, area, bulk resistivity, and line resistance of the four contacts shown in Figure 9.

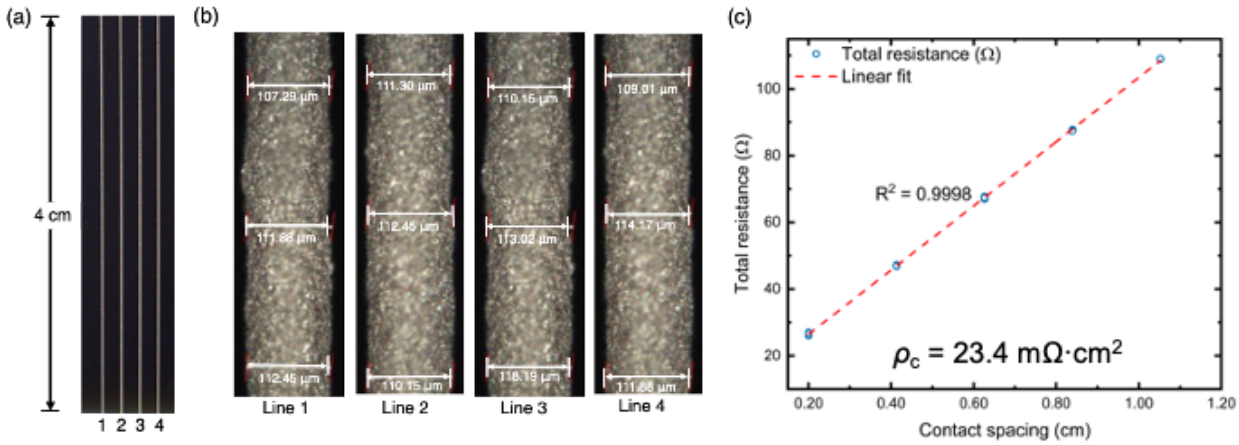

Figure 9. (a) Visible image of the Ag contacts printed on a portion of the textured silicon substrate featuring ITO and a-Si:H thin films. (b) Optical microscopy images showing a magnified view of the lines. (c) Results from the TLM measurements performed on an identical substrate using the same Ag printing and laser sintering processing conditions.

Table 2. Average line width, height, area, bulk resistivity, and line resistance for the four lines shown in Figure 4.

Line #	Average Line Width (µm)	Average of Maximum Height (µm)	Average Cross Sectional Area ($µm^2$)	Bulk Resistivity (µΩ•cm)	Average Line Resistance (mΩ/cm)
1	111	10.6	1168	6.49	556
2	111	10.7	1195	6.65	557
3	114	11.6	1324	6.66	503
4	112	10.5	1173	6.20	527

We have found that the microstructure plays an important role in dictating the conductivity of the Ag lines. The Ag paste we are now using features Ag nanoflakes and nanoparticles. To ensure good conductivity, a porous bridge network must be formed wherein the flakes and particles coalesce and leave behind. This seems counterintuitive, but makes sense if you consider the printed flakes and particles are not properly bonded in the as-deposited state and need to merge together to limit scattering at interfaces. A high electron mobility is dependent on minimizing scattering events and the porous bridge network provides low resistance pathways for current flow that minimize this scattering loss.

Figure 10 shows cross-sectional SEM images of two contacts printed with the same Ag paste. The Ag contact was printed with a higher flow rate leading to a taller contact (18.2 µm). This sounds good in principle, but when the contact is too tall, the CO_2 laser sintering process cannot effectively sinter the entire contact. The other contact printed with a lower flow rate is 15.4 µm, not quite as thick, but is effectively sintered leading to

the desired porous bridge network and much lower resistivity, 7.1 μΩ·cm versus 31.5 μΩ·cm for the other contact.

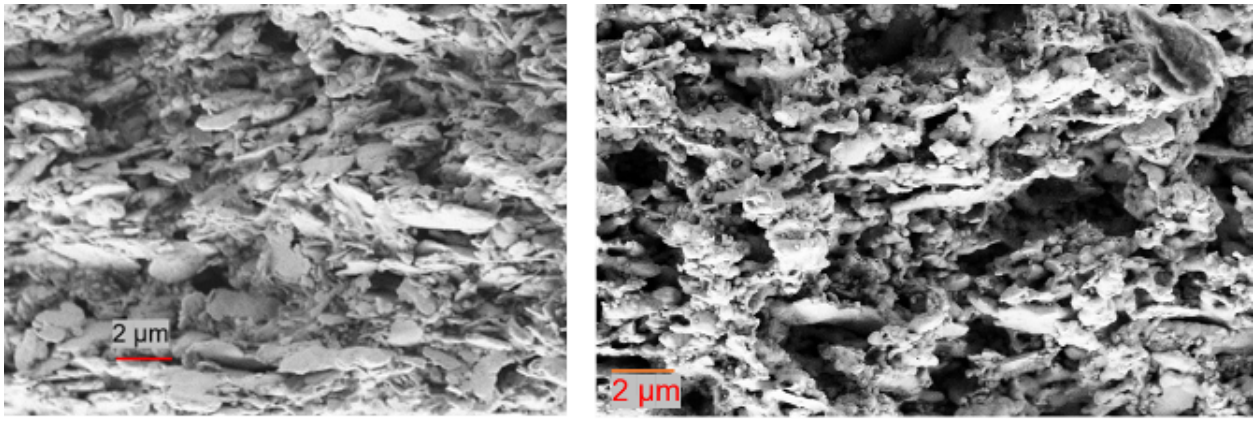

Figure 10. Cross-sectional SEM images of (left) a taller Ag contact that is improperly sintered, leading to a high bulk resistivity (31.5 μΩ·cm), and (right) a shorter Ag contact that is properly sintered, yielding a lower bulk resistivity (7.1 μΩ·cm).

EDS analysis has also been performed on the printed contact. The EDS spectra of the laser printed Ag line in Figure 11 refers to the deposition of Ag without significant amounts of carbon and oxygen present in the contact material.

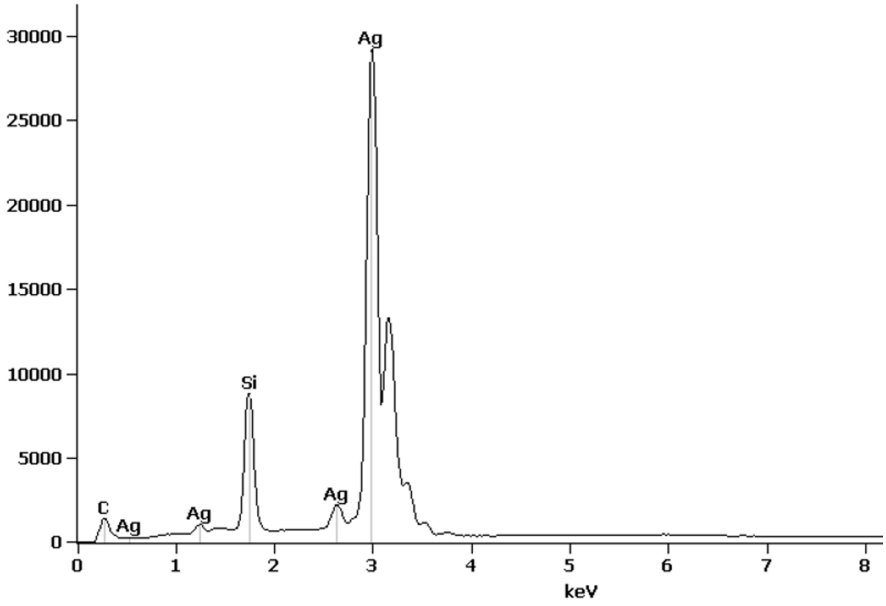

Figure 11. EDS spectra of the laser printed silver contact showing the deposition of silver with very low/no impurities.

The team has also continued to use photoluminescence (PL) imaging to ensure the laser sintering process does not lead to any degradation in the passivation quality of the a-Si:H(i)/c-Si(n) interface. It is well known that if an a-Si:H(i)/c-Si(n) interface exceeds a

temperature of 200°C for an appreciable amount of time, epitaxy can occur. Ultimately, this leads to the formation of crystallographic defects (e.g., dislocations, nanotwins) that act as deep-level Shockley-Read-Hall recombination centers [61]. This lowers the effective carrier lifetime and therefore Δn. PL intensity provides a great way to probe the local Δn and is an effective way to monitor local increases in recombination. Figure 12 below shows PL images of the same sample before and after our Ag printing and sintering. The flipped PL image on the right shows no local darkening in the PL, indicating there is no new added recombination after printing and sintering.

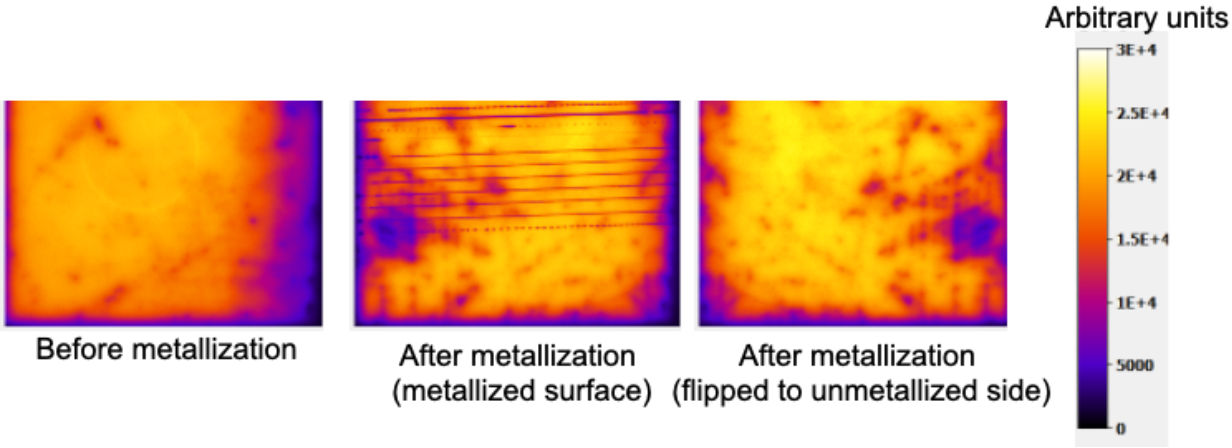

Figure 12. PL images of the same sample before and after metallization. The image on the far right shows there does not appear to be any increase in recombination due to the printing and sintering of the Ag lines. If there were, localized darkening would be evident in the flipped image.

3.1.3 Optical and Thermal Modeling of the Laser Sintering of Silver

An optical and thermal model of the laser sintering process was also developed in this project and validated with the experimental results shown above. This model enables accurate prediction of the optical absorption occurring within the printed Ag contact and the resulting heat transfer that is responsible for the nanoparticle sintering. A detailed description of this model can be found here [17].

3.2 Printed Poly-Si Contacts on APCVD Poly-Si Thin Films

3.2.1 APCVD Poly-Si Thin Films

As mentioned previously and illustrated in Figure 1b, the printed poly-Si lines are formed on top of APCVD poly-Si films with an underlying SiO_x passivation layer. The as-deposited APCVD doped poly-Si passivating films described in section 3.2 were annealed at different temperatures to activate the surface passivation quality. The change in the composition, microstructure, and electrical properties of the thin doped poly-Si layers due to different deposition temperature, PH_3 gas ratio, and annealing temperature has been described in detail in [18].

Figure 13a and 13b demonstrate the average J_0 and iV_{OC} of the APCVD poly-Si samples after the high temperature annealing. Surface passivation of the poly-Si contact starts to improve with the annealing process. Annealing at 820°C reduces the J_0 value and improves the iV_{OC} of the contact. Comparatively lower J_0 and higher iV_{OC} have been observed for the batches with higher P concentration after annealing at 820°C for

30 minutes as low P concentration in poly-Si layer results in low field effect passivation at the interface [62]. Passivation quality keeps improving with the increase of annealing temperature up to 850°C. Figure 13a shows that the J_0 values of all the batches reach their lowest values when annealed at 850°C for 30 minutes. This annealing condition also resulted in the highest iV_{OC} for all the batches except for the batch deposited at 750°C with 9.09% PH_3 ratio.

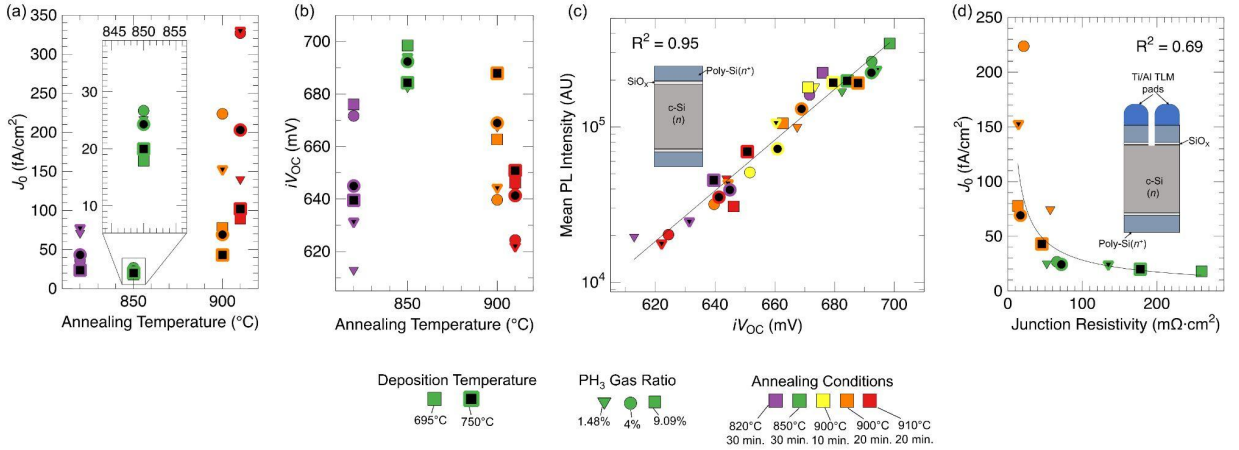

Figure 13. (a) Saturation current density (J_0) of the poly-Si samples for different annealing conditions. (b) Implied open-circuit voltage (iV_{OC}) of the poly-Si samples for different annealing conditions. (c) Mean photoluminescence (PL) intensity versus iV_{OC} of the symmetrical samples annealed for different conditions on a log-linear plot. (d) J_0 versus junction resistivity of the poly-Si contacts annealed at 850°C and 900°C.

The excellent surface passivation at 850°C originates from the enhancement of the chemical passivation and the field effect passivation. Chemical passivation improvement emerges from the reorientation of the SiO_x bonding at the interface at this temperature [63]. Moreover, increased active dopant concentration in the poly-Si layer and dopant diffusion through the SiO_x layer into the c-Si increases the band bending at the interface [64] and thus enhances the field effect passivation. The combination of these mechanisms provides this excellent surface passivation after annealing at 850°C for 30 minutes. The poly-Si layer with higher P concentration demonstrates the lower J_0. The lowest J_0 and the highest iV_{OC} have been achieved for the poly-Si batch deposited at 695°C with 9.09% PH_3 ratio. J_0 as low as 13 fA/cm2 and iV_{OC} as high as 701 mV have been achieved for this batch without any hydrogenation process. Raising an annealing temperature more than 850°C increases the J_0 and lowers the iV_{OC} (Figure 13a,b). This might be because of the excessive dopant diffusion into the c-Si due to the high annealing temperature which increases the Auger recombination. Moreover, other studies have shown pinholes and damage formation in the SiO_x layer when annealed at this high temperature which degrades the chemical passivation [34], [65], [66]. In addition, hydrogen at the poly-Si/SiO_x interface effuses out during the annealing process which deteriorates the chemical passivation of the interface.

The annealed samples were hydrogenated using a hydrogen-rich atomic layer deposition (ALD) Al_2O_3 layer to improve the surface passivation quality even further. During annealing after Al_2O_3 deposition, hydrogen from the Al_2O_3 layer diffuses to the poly-Si/SiO_x interface. Van de Loo et al. demonstrated [67] that the hydrogen concentration increased significantly at the poly-Si/SiO_x interface due to the hydrogen

diffusion from the H-rich Al_2O_x layer. The supplied hydrogen improves the surface passivation quality by passivating defects and dangling bonds at the c-Si absorber surface [67]. The iV_{OC} of the poly-Si contact on planar wafers improves from 701 mV to 712 mV after hydrogenation. The J_0 of 3 fA/cm^2 has been achieved for the corresponding batch after hydrogenation which indicates an excellent surface passivation quality of the contact. For the poly-Si contact on the textured samples, J_0 as low as 17 fA/cm^2 and iV_{OC} of 706 mV have been achieved after hydrogenation.

Figure 13d presents the junction resistivity of the poly-Si contact annealed in different conditions. Junction resistivity values less than 15 mΩ·cm^2 have been realized for the poly-Si samples annealed at 900°C, but this annealing condition causes degradation in surface passivation quality. For the optimized annealing condition (850°C for 30 minutes), junction resistivity values of around 50 mΩ·cm^2 have been achieved, which is still low enough for full area contacts. Figure 13d illustrates that J_0 and junction resistivity of the APCVD poly-Si contacts are related through an exponential decay, wherein lower junction resistivity means higher J_0. Higher dopant diffusion into the c-Si and damage/pinhole formation in the SiO_x layer facilitates carrier transport through the contact and therefore yields lower junction resistivity [34]. On the other hand, excessive dopant diffusion into the c-Si and any damage or pinhole formation in SiO_x layer lowers the J_0. Because of these reasons, J_0 has an inverse relationship to the junction resistivity. For *in situ* P-doped APCVD poly-Si(*n*), though increasing dopant concentration improves the surface passivation quality, but too much dopant results in very high junction resistivity by decreasing the grain size and the dopant mobility which lowers the carrier selectivity of the contact. These factors should be considered during selecting a carrier selective contact.

3.2.2 Poly-Si Contact Printing Results

The team is able to print Si lines by laser printing of arsenic doped Si nanoparticles ink.

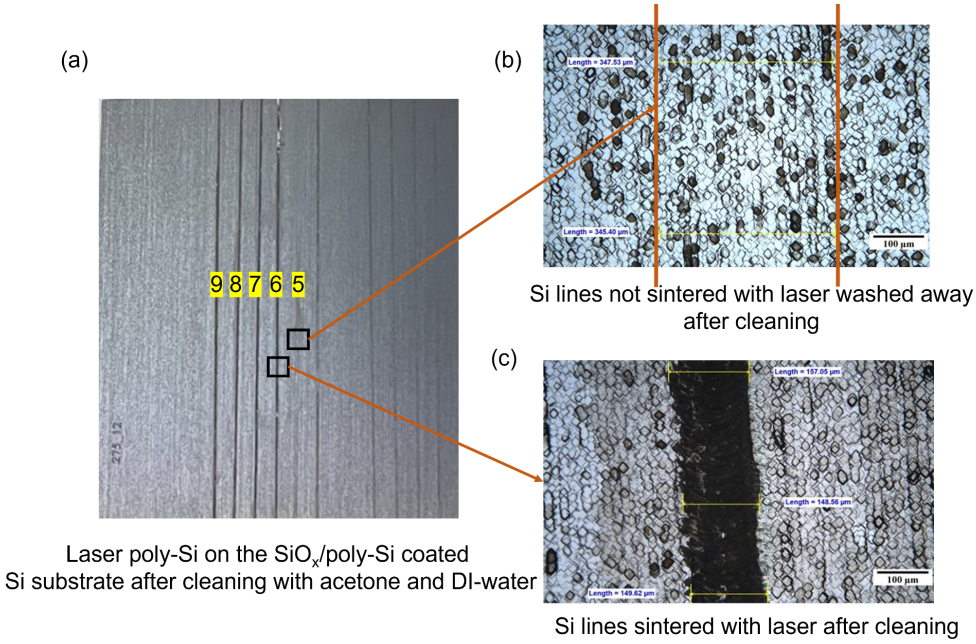

Figure 15. Laser printed poly-Si lines after cleaning with acetone and DI water.

The substrates for this printing was the c-Si coated with DI-O_3 passivated APCVD P-doped poly-Si(*n*) contact. Figure 15 shows the Si lines printed using 1064 nm Nd:YAG laser. The sample was cleaned using acetone and DI water after printing. Figure 15 shows that the line which was not sintered using the laser was washed away after cleaning whereas the line sintered with 13.8 W laser remained on the substrate.

The influence of laser power has been investigated on the poly-Si line deposition quality. As from Figure 16 we can see that the line width and the deposition quality significantly depend on the laser power. The printed poly-Si line width increases with the increase of the laser power.

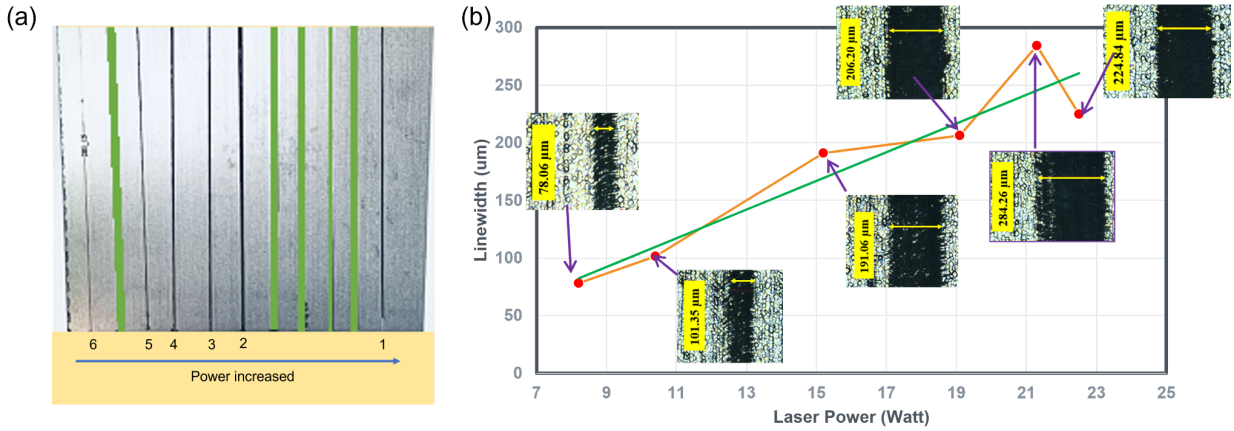

Figure 16. (a) Si lines printed using different laser power. Laser power increased from line 6 to line 1 during deposition. (b) Line width of the Si lines in (a) vs laser power plot. The six points represent the six lines in (a).

Laser power also influences the passivation quality of the SiO_x/APCVD poly-Si contact as 1064 nm is absorbed in the Si material. Therefore, optimized laser power that prints Si without damaging the passivation quality has been determined.

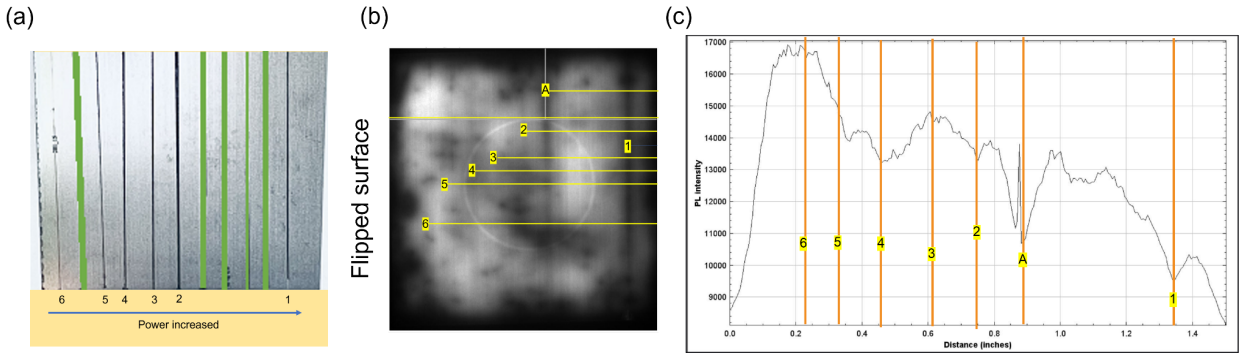

Figure 17. (a) Si lines printed using different laser power. Laser power increased from line 6 to line 1 during deposition. (b) Uncalibrated PL image of the flipped surface of the substrate in (a). The number indicates the position of the lines presented in (a), and (c) PL intensity counts on the position of the different Si lines.

Figure 17 shows that the PL intensity drops significantly at the position where lines (line 1, A, and 2) are deposited using higher laser power. But the regions sintered with low laser power (< 20 W) show very little to no drop in the PL count. Ultimately, many challenges still remain, but this work represents an important step in the direction of

realizing the printing of localized poly-Si contacts as a means of limiting metal-induced recombination and parasitic optical absorption in TOPCon and POLO cells.

4. Conclusions

This work demonstrates a contact printing technique for SHJ solar cells using laser energy. Metal contact with line width as low as ≃ 111 μm and bulk resistivity as low as ≃ 7.0 μΩ·cm has been deposited without any damage in the amorphous silicon passivating layer using this printing technique. Average line height of 20 μm has been achieved using this contact printing technique. The achieved line width, bulk resistivity, and line height values are very close to the project goals (line width 50 μm, line height 20 μm, and bulk resistivity 5 μΩ·cm). Line width can be reduced more by using a needle with smaller inner diameter but that might cause needle clogging during dispensing the silver paste. In this case, using a nozzle with a narrow tiphead might be an alternative.

In this work, a silicon oxide passivated APCVD deposited phosphorus doped poly-Si passivating electron selective contact has been developed. The effect of deposition process parameters and post-deposition treatments have studied on the properties and performance of the passivating contact. The APCVD poly-Si passivating contact has demonstrated J_0 less than 5 fA/cm^2 after annealing and hydrogenation.

Additionally, silicon lines have been printed on the SiO_x and APCVD poly-Si passivating layer coated *n*-type c-Si wafers by sintering As-doped Si nanoparticles ink using Nd:YAG laser. Impact of laser power on the line width and the passivation quality have been observed.

5. Budget and Schedule

The overall project spending aligned pretty well with the planned budget, as shown the table below. The schedule was delayed a bit at the beginning of the project due to the COVID-19 pandemic, but the team still managed to remain productive and complete the majority of the key milestones.

Spending Summary by Budget Category

	Approved Budget per SF-424A				Actual Expenses		
Budget Categories per SF-424a	BP 1	BP 2	BP 3	Total	This Quarter	Cumulative	%
a. Personnel	$104,400			$104,400	$29,411	$103,052	99%
b. Fringe Benefits	$17,727			$17,727	$9,117	$19,018	107%
c. Travel	$3,592			$3,592	$0	$0	0%
d. Equipment	$0			$0	$0	$0	0%
e. Supplies	$21,978			$21,978	-$2,083	$37,200	169%
f. Contractual	$0			$0	$0	$0	0%

g. Construction	$0			$0	$0	$0	0%
h. Other	$26,422			$26,422	$0	$13,929	53%
i. Total Direct Charges	**$174,119**	**$0**	**$0**	**$174,119**	**$36,445**	**$173,200**	99%
j. Indirect Charges	$75,881			**$75,881**	$17,858	$76,800	101%
k. Total Charges	**$250,000**	**$0**	**$0**	**$250,000**	**$54,304**	**$250,000**	100%
DOE Share	$200,000	0		$200,000	**$54,304**	**$200,000**	100%
Cost Share	$50,000	0		$50,000	$0	$50,000	100%
Cost Share Percentage	20.0%	0%	0%	20.0%	0.0%	20.0%	100%

6. Path Forward

In this work, line width as low as ≃ 111 µm has been achieved using silver paste. The line width can be reduced more by using a needle with a smaller diameter, but this might cause needle clogging during dispensing the silver paste. The system can be improved using a nozzle with narrow tiphead to print metal contact with smaller line width. The achieved bulk resistivity and contact resistivity can be reduced by using higher laser power as higher laser energy improves the sintering of the metal contact. The contact resistivity can be improved by filling the porous regions at the metal contact and textured substrate interface. By printing the first few layers using liquid ink with low viscosity followed by printing the heavily viscous metal paste might help to reduce the porous region at the interface and decrease the contact resistivity.

Another promising candidate for the metallization of SHJ solar cells is copper (Cu) contact due to lower materials cost of Cu compared to Ag. Metallization techniques like electroplating of Cu have been explored as alternatives to Ag [68], [69], [70, p. 1]. The laser printing technique developed in this work can also be used to print Cu contact on SHJ cells. In this work, Cu contact has been printed using a copper screen paste (82.1% solid content) from Novacentrix.

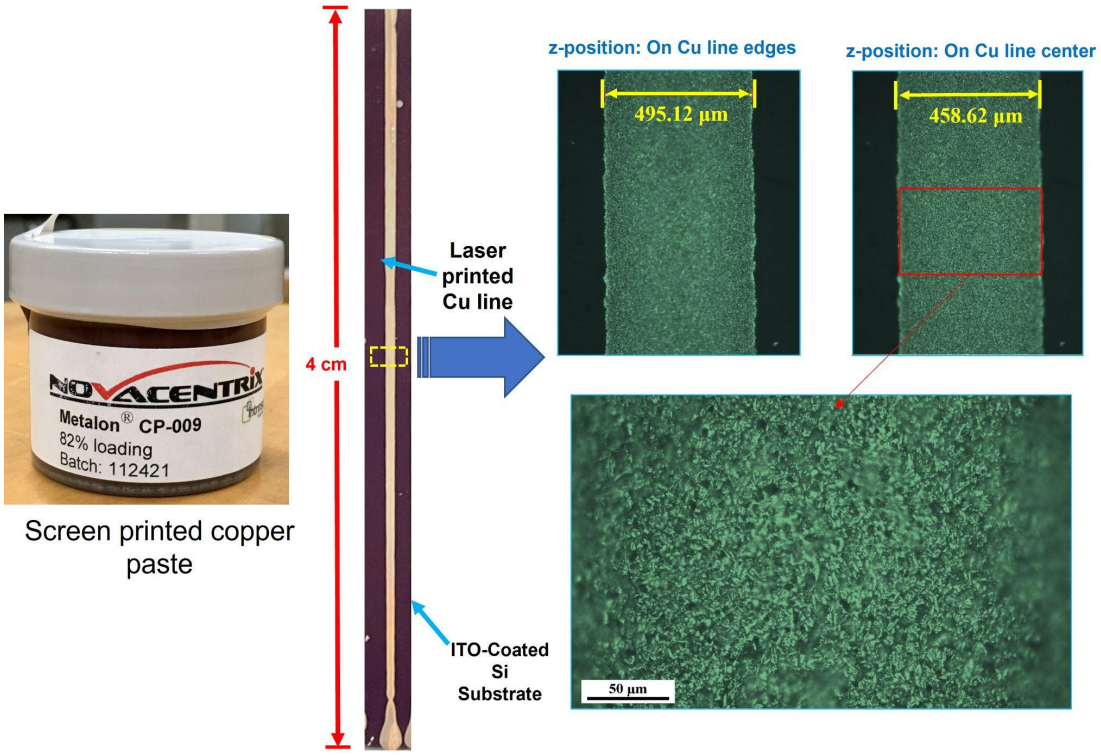

The paste was dispensed through a needle with 230 µm inner diameter and sintered using 8.9 W 10.6 µm CO_2 laser. The average width and height of the printed line are 467.87 µm and 30 µm, respectively with line resistance of 3.8 Ω/cm. Further investigation and process parameters optimization are required for lowering the line width and line resistance of the printed copper contact.

This work demonstrates that polysilicon contacts can be deposited and annealed using this laser deposition process, but challenges remain. More process parameter optimization and characterization are required to further improve the silicon line quality and to understand the process-structure-properties relationships of the printed contact.

7. Information Dissemination

Our team at UCF made every effort to disseminate our findings throughout the course of this project. A list of the published works is given below.

7.1 Journal Publications

J3. Mousumi JF, Bougdid Y, Kulkarni G, Kar A, Kumar R, Davis KO. Printing and Laser Sintering of Silver Contacts for Crystalline Silicon Heterojunction Solar Cells. In preparation.

J2. Li T, Davis KO, Kumar R, Kar A. Diffraction and Thermal Effect of a Bessel-Gaussian Laser for Ag Nanoparticle Deposition. *Optics Express* 2022. https://doi.org/10.1364/OE.455313

J1. Mousumi JF, Gregory G, Ganesan JP, Nunez C, Provancha K, Seren S, Zunft H, Jurca T, Banerjee P, Kar A, Kumar R, Davis KO. Process–Structure–Properties Relationships of Passivating, Electron-Selective Contacts Formed by Atmospheric Pressure Chemical Vapor Deposition of Phosphorus-Doped Polysilicon. *physica status solidi (RRL) - Rapid Research Letters* 2022; 16: 2100639. https://doi.org/10.1002/pssr.202100639

7.2 Conference Proceedings

C2. Mousumi JF, Gregory G, Nunez C, Ganesan JP, Provancha K, Seren S, Banerjee P, Davis KO. Influence of Process Parameters on the Surface Passivation Quality of Phosphorus Doped Polysilicon Contacts Deposited by APCVD. *48th IEEE Photovoltaic Specialists Conference*, Fort Lauderdale, FL, 2021. https://doi.org/10.1109/PVSC43889.2021.9518784

C1. Mousumi JF, Li T, Kulkarni G, Kar A, Kumar R, Davis KO. Localized Laser Printing and Sintering of Silver Nanoparticles for Silicon Solar Cell Metallization. *48th IEEE Photovoltaic Specialists Conference*, Fort Lauderdale, FL, 2021. https://doi.org/10.1109/PVSC43889.2021.9518857

Acknowledgements

This material is based upon work supported by the U.S. Department of Energy's Office of Energy Efficiency and Renewable Energy (EERE) under the Solar Energy Technologies Office Award Number DE-EE0008980. The authors would also like to thank the many collaborators, including Dr. Sven Seren, Dr. Titel Jurca, Dr. Parag Banerjee, Geoffrey Gregory, Jeya Prakash Ganesan, Christian Nunez, Kenneth Provancha, and Heiko Zunft.

Disclaimer

References

[1] T. Fellmeth, A. Born, A. Kimmerle, F. Clement, D. Biro, and R. Preu, “Recombination at Metal-Emitter Interfaces of Front Contact Technologies for Highly Efficient Silicon Solar Cells,” *Energy Procedia*, vol. 8, pp. 115–121, Jan. 2011, doi: 10.1016/j.egypro.2011.06.111.

[2] J. Deckers, M. Debucquoy, I. Gordon, R. Mertens, and J. Poortmans, “Avoiding

Parasitic Current Flow Through Point Contacts in Test Structures for QSSPC Contact Recombination Current Measurements," *Photovoltaics, IEEE Journal of*, vol. 5, pp. 276–281, 2015, doi: 10.1109/JPHOTOV.2014.2359731.

[3] V. Shanmugam, T. Mueller, A. G. Aberle, and J. Wong, "Determination of metal contact recombination parameters for silicon wafer solar cells by photoluminescence imaging," *Solar Energy*, vol. 118, pp. 20–27, 2015, doi: 10.1016/j.solener.2015.05.010.

[4] D. Inns, "Understanding Metal Induced Recombination Losses in Silicon Solar Cells with Screen Printed Silver Contacts," *Energy Procedia*, vol. 98, pp. 23–29, Nov. 2016, doi: 10.1016/j.egypro.2016.10.077.

[5] R. Dumbrell, M. K. Juhl, T. Trupke, and Z. Hameiri, "Extracting Metal Contact Recombination Parameters From Effective Lifetime Data," *IEEE Journal of Photovoltaics*, vol. 8, no. 6, pp. 1413–1420, Nov. 2018, doi: 10.1109/JPHOTOV.2018.2861761.

[6] S. Guo, S. Johnston, W. V. Schoenfeld, and K. O. Davis, "Metal Induced Recombination Parameter Extraction using High Resolution Photoluminescence Imaging for Silicon Solar Cells," in *2018 IEEE 7th World Conference on Photovoltaic Energy Conversion (WCPEC) (A Joint Conference of 45th IEEE PVSC, 28th PVSEC 34th EU PVSEC)*, Jun. 2018, pp. 3743–3745. doi: 10.1109/PVSC.2018.8547945.

[7] M. Li, J. Wong, N. Chen, A. G. Aberle, and R. Stangl, "Determination of Metallization-Induced Recombination Losses of Screen-Printed Silicon Solar Cell Contacts and Their Dependence on the Doping Profile," *IEEE Journal of Photovoltaics*, vol. 8, no. 6, pp. 1470–1477, 2018, doi: 10.1109/JPHOTOV.2018.2866177.

[8] M. Li, N. Iqbal, X. Lin, Z. Yang, and K. Davis, "Characterization of the Metallization Induced Recombination Losses in Industrial Silicon Solar Cells," in *2019 IEEE 46th Photovoltaic Specialists Conference (PVSC)*, Chicago, IL, USA: IEEE, Jun. 2019, pp. 2769–2773. doi: 10.1109/PVSC40753.2019.8981257.

[9] M. Li *et al.*, "A Comprehensive Evaluation of Contact Recombination and Contact Resistivity Losses in Industrial Silicon Solar Cells," *IEEE Journal of Photovoltaics*, vol. 10, no. 5, pp. 1277–1282, 2020, doi: 10.1109/JPHOTOV.2020.3003792.

[10] M. S. Jeong *et al.*, "Numerical Simulation Analysis of Ag Crystallite Effects on Interface of Front Metal and Silicon in the PERC Solar Cell," *Energies*, vol. 14, no. 3, Art. no. 3, Jan. 2021, doi: 10.3390/en14030592.

[11] S. De Wolf, A. Descoeudres, Z. C. Holman, and C. Ballif, "High-efficiency Silicon Heterojunction Solar Cells: A Review," *Green*, vol. 2, 2012, doi: 10.1515/green-2011-0018.

[12] K. O. Davis and W. V. Schoenfeld, "Engineered Interfaces Using Surface and Contact Passivation in Silicon Solar Cells," *Electrochem. Soc. Interface*, vol. 27, no. 1, pp. 63–66, Jan. 2018, doi: 10.1149/2.F07181if.

[13] J. Melskens, B. W. H. van de Loo, B. Macco, L. E. Black, S. Smit, and W. M. M. Kessels, "Passivating Contacts for Crystalline Silicon Solar Cells: From Concepts and Materials to Prospects," *IEEE Journal of Photovoltaics*, vol. 8, no. 2, pp. 373–388, Mar. 2018, doi: 10.1109/JPHOTOV.2018.2797106.

[14] T. G. Allen, J. Bullock, X. Yang, A. Javey, and S. D. Wolf, "Passivating contacts for crystalline silicon solar cells," *Nat Energy*, vol. 4, pp. 914–928, Sep. 2019, doi:

10.1038/s41560-019-0463-6.
[15] D. Yan *et al.*, “Polysilicon passivated junctions: The next technology for silicon solar cells?,” *Joule*, vol. 5, no. 4, pp. 811–828, Apr. 2021, doi: 10.1016/j.joule.2021.02.013.
[16] A. Razzaq, T. G. Allen, W. Liu, Z. Liu, and S. De Wolf, “Silicon heterojunction solar cells: Techno-economic assessment and opportunities,” *Joule*, vol. 6, no. 3, pp. 514–542, Mar. 2022, doi: 10.1016/j.joule.2022.02.009.
[17] T. Li, K. O. Davis, R. Kumar, and A. Kar, “Diffraction and thermal effect of a Bessel-Gaussian laser for Ag nanoparticle deposition,” *Opt. Express, OE*, vol. 30, no. 11, pp. 19246–19272, May 2022, doi: 10.1364/OE.455313.
[18] J. F. Mousumi *et al.*, “Process–Structure–Properties Relationships of Passivating, Electron‐Selective Contacts Formed by Atmospheric Pressure Chemical Vapor Deposition of Phosphorus‐Doped Polysilicon,” *Physica Rapid Research Ltrs*, vol. 16, no. 5, p. 2100639, May 2022, doi: 10.1002/pssr.202100639.
[19] A. Louwen, W. van Sark, R. Schropp, and A. Faaij, “A cost roadmap for silicon heterojunction solar cells,” *Solar Energy Materials and Solar Cells*, vol. 147, pp. 295–314, 2016, doi: 10.1016/j.solmat.2015.12.026.
[20] J. Geissbühler *et al.*, “22.5% efficient silicon heterojunction solar cell with molybdenum oxide hole collector,” *Applied Physics Letters*, vol. 107, no. 8, 2015, doi: 10.1063/1.4928747.
[21] D. Sacchetto *et al.*, “ITO/MoOx/a-Si:H(i) Hole-Selective Contacts for Silicon Heterojunction Solar Cells: Degradation Mechanisms and Cell Integration,” *IEEE Journal of Photovoltaics*, vol. 7, no. 6, pp. 1584–1590, Nov. 2017, doi: 10.1109/JPHOTOV.2017.2756066.
[22] H. Ali *et al.*, “Thermal Stability of Hole-Selective Tungsten Oxide: In Situ Transmission Electron Microscopy Study,” *Scientific Reports*, vol. 8, no. 1, p. 12651, Aug. 2018, doi: 10.1038/s41598-018-31053-w.
[23] H. Ali *et al.*, “In Situ Transmission Electron Microscopy Study of Molybdenum Oxide Contacts for Silicon Solar Cells,” *physica status solidi (a)*, vol. 216, no. 7, p. 1800998, 2019, doi: 10.1002/pssa.201800998.
[24] S. Essig *et al.*, “Toward Annealing-Stable Molybdenum-Oxide-Based Hole-Selective Contacts For Silicon Photovoltaics,” *Solar RRL*, vol. 2, no. 4, p. 1700227, 2018, doi: 10.1002/solr.201700227.
[25] H. Ali *et al.*, “Transmission Electron Microscopy and Electron Energy-Loss Spectroscopy Studies of Hole-Selective Molybdenum Oxide Contacts in Silicon Solar Cells,” *ACS Appl. Mater. Interfaces*, vol. 11, no. 46, pp. 43075–43080, Nov. 2019, doi: 10.1021/acsami.9b12703.
[26] G. Gregory, M. Wilson, H. Ali, and K. O. Davis, “Thermally Stable Molybdenum Oxide Hole-Selective Contacts Deposited using Spatial Atomic Layer Deposition,” in *2018 IEEE 7th World Conference on Photovoltaic Energy Conversion (WCPEC) (A Joint Conference of 45th IEEE PVSC, 28th PVSEC 34th EU PVSEC)*, Jun. 2018, pp. 2006–2009. doi: 10.1109/PVSC.2018.8547343.
[27] G. Gregory, C. Feit, Z. Gao, P. Banerjee, T. Jurca, and K. O. Davis, “Improving the Passivation of Molybdenum Oxide Hole-Selective Contacts with 1 nm Hydrogenated Aluminum Oxide Films for Silicon Solar Cells,” *physica status solidi (a)*, vol. 217, no. 15, p. 2000093, 2020, doi: 10.1002/pssa.202000093.

[28] L. Neusel, M. Bivour, and M. Hermle, “Selectivity issues of MoOx based hole contacts,” *Energy Procedia*, vol. 124, 2017, doi: 10.1016/j.egypro.2017.09.268.
[29] F. Feldmann, M. Bivour, C. Reichel, H. Steinkemper, M. Hermle, and S. W. Glunz, “Tunnel oxide passivated contacts as an alternative to partial rear contacts,” *Solar Energy Materials and Solar Cells*, vol. 131, pp. 46–50, Dec. 2014, doi: 10.1016/j.solmat.2014.06.015.
[30] F. Feldmann *et al.*, “Charge carrier transport mechanisms of passivating contacts studied by temperature-dependent J-V measurements,” *Solar Energy Materials and Solar Cells*, vol. 178, pp. 15–19, May 2018, doi: 10.1016/j.solmat.2018.01.008.
[31] F. Feldmann *et al.*, “A Study on the Charge Carrier Transport of Passivating Contacts,” *IEEE J. Photovoltaics*, vol. 8, no. 6, pp. 1503–1509, Nov. 2018, doi: 10.1109/JPHOTOV.2018.2870735.
[32] N. Folchert, M. Rienäcker, A. A. Yeo, B. Min, R. Peibst, and R. Brendel, “Temperature-dependent contact resistance of carrier selective Poly-Si on oxide junctions,” *Solar Energy Materials and Solar Cells*, vol. 185, pp. 425–430, Oct. 2018, doi: 10.1016/j.solmat.2018.05.046.
[33] A. S. Kale *et al.*, “Effect of silicon oxide thickness on polysilicon based passivated contacts for high-efficiency crystalline silicon solar cells,” *Solar Energy Materials and Solar Cells*, vol. 185, pp. 270–276, Oct. 2018, doi: 10.1016/j.solmat.2018.05.011.
[34] R. Peibst *et al.*, “Working principle of carrier selective poly-Si/c-Si junctions: Is tunnelling the whole story?,” *Solar Energy Materials and Solar Cells*, vol. 158, pp. 60–67, Dec. 2016, doi: 10.1016/j.solmat.2016.05.045.
[35] Z. Zhang *et al.*, “Carrier transport through the ultrathin silicon-oxide layer in tunnel oxide passivated contact (TOPCon) c-Si solar cells,” *Solar Energy Materials and Solar Cells*, vol. 187, pp. 113–122, Dec. 2018, doi: 10.1016/j.solmat.2018.07.025.
[36] F. Haase *et al.*, “Laser contact openings for local poly-Si-metal contacts enabling 26.1%-efficient POLO-IBC solar cells,” *Solar Energy Materials and Solar Cells*, vol. 186, pp. 184–193, Nov. 2018, doi: 10.1016/j.solmat.2018.06.020.
[37] S. Schäfer *et al.*, “26%-efficient and 2 cm narrow interdigitated back contact silicon solar cells with passivated slits on two edges,” *Solar Energy Materials and Solar Cells*, vol. 200, p. 110021, Sep. 2019, doi: 10.1016/j.solmat.2019.110021.
[38] H. Fujiwara, T. Kaneko, and M. Kondo, “Optimization of interface structures in crystalline silicon heterojunction solar cells,” *Solar Energy Materials and Solar Cells*, vol. 93, no. 6–7, pp. 725–728, Jun. 2009, doi: 10.1016/j.solmat.2008.09.007.
[39] H. Park *et al.*, “Passivation quality control in poly-Si/SiO /c-Si passivated contact solar cells with 734 mV implied open circuit voltage,” *Solar Energy Materials and Solar Cells*, vol. 189, pp. 21–26, Jan. 2019, doi: 10.1016/j.solmat.2018.09.013.
[40] M. K. Stodolny *et al.*, “Material properties of LPCVD processed n-type polysilicon passivating contacts and its application in PERPoly industrial bifacial solar cells,” *Energy Procedia*, vol. 124, pp. 635–642, Sep. 2017, doi: 10.1016/j.egypro.2017.09.250.
[41] N. Nandakumar *et al.*, “Approaching 23% with large‐area monoPoly cells using screen‐printed and fired rear passivating contacts fabricated by inline PECVD,” *Prog Photovolt Res Appl*, p. pip.3097, Dec. 2018, doi: 10.1002/pip.3097.
[42] A. Richter, J. Benick, F. Feldmann, A. Fell, M. Hermle, and S. W. Glunz, “n-Type

Si solar cells with passivating electron contact: Identifying sources for efficiency limitations by wafer thickness and resistivity variation," *Solar Energy Materials and Solar Cells*, vol. 173, pp. 96–105, Dec. 2017, doi: 10.1016/j.solmat.2017.05.042.

[43] J.-I. Polzin, F. Feldmann, B. Steinhauser, M. Hermle, and S. Glunz, "Realization of TOPCon using industrial scale PECVD equipment," Lausanne, Switzerland, 2018, p. 040018. doi: 10.1063/1.5049281.

[44] D. Yan, A. Cuevas, S. P. Phang, Y. Wan, and D. Macdonald, "23% efficient p-type crystalline silicon solar cells with hole-selective passivating contacts based on physical vapor deposition of doped silicon films," *Appl. Phys. Lett.*, vol. 113, no. 6, p. 061603, Aug. 2018, doi: 10.1063/1.5037610.

[45] S. Duttagupta, N. Nandakumar, P. Padhamnath, J. K. Buatis, R. Stangl, and A. G. Aberle, "monoPoly^{TM} cells: Large-area crystalline silicon solar cells with fire-through screen printed contact to doped polysilicon surfaces," *Solar Energy Materials and Solar Cells*, vol. 187, pp. 76–81, Dec. 2018, doi: 10.1016/j.solmat.2018.05.059.

[46] D. Yan, A. Cuevas, J. Bullock, Y. Wan, and C. Samundsett, "Phosphorus-diffused polysilicon contacts for solar cells," *Solar Energy Materials and Solar Cells*, vol. 142, pp. 75–82, Nov. 2015, doi: 10.1016/j.solmat.2015.06.001.

[47] G. Limodio *et al.*, "Implantation‐based passivating contacts for crystalline silicon front/rear contacted solar cells," *Prog Photovolt Res Appl*, vol. 28, no. 5, pp. 403–416, May 2020, doi: 10.1002/pip.3250.

[48] S. Reiter *et al.*, "Parasitic Absorption in Polycrystalline Si-layers for Carrier-selective Front Junctions," *Energy Procedia*, vol. 92, pp. 199–204, Aug. 2016, doi: 10.1016/j.egypro.2016.07.057.

[49] G. Yang *et al.*, "Oxygen‐alloyed poly‐Si passivating contacts for high‐thermal budget c‐Si heterojunction solar cells," *Progress in Photovoltaics*, vol. 30, no. 2, pp. 141–151, Feb. 2022, doi: 10.1002/pip.3472.

[50] B. Kafle, B. S. Goraya, S. Mack, F. Feldmann, S. Nold, and J. Rentsch, "TOPCon – Technology options for cost efficient industrial manufacturing," *Solar Energy Materials and Solar Cells*, vol. 227, p. 111100, Aug. 2021, doi: 10.1016/j.solmat.2021.111100.

[51] L. E. Black, K. M. Provancha, and K. R. McIntosh, "Surface Passivation of Crystalline Silicon by APCVD Aluminium Oxide," presented at the 26th European Photovoltaic Solar Energy Conference and Exhibition, 2011, pp. 1120–1124. doi: 10.4229/26thEUPVSEC2011-2DO.1.2.

[52] L. E. Black, T. Allen, A. Cuevas, K. R. McIntosh, B. Veith, and J. Schmidt, "Thermal stability of silicon surface passivation by APCVD Al2O3," *Solar Energy Materials and Solar Cells*, vol. 120, pp. 339–345, 2013, doi: 10.1016/j.solmat.2013.05.048.

[53] K. O. Davis *et al.*, "Influence of precursor gas ratio and firing on silicon surface passivation by APCVD aluminium oxide," *physica status solidi (RRL) – Rapid Research Letters*, vol. 7, pp. 942–945, 2013, doi: 10.1002/pssr.201308092.

[54] K. O. Davis *et al.*, "Improved control of the phosphorous surface concentration during in-line diffusion of c-Si solar cells by APCVD," *physica status solidi (RRL) - Rapid Research Letters*, vol. 7, pp. 319–321, 2013, doi: 10.1002/pssr.201307020.

[55] K. O. Davis, K. Jiang, D. Habermann, and W. V. Schoenfeld, "Tailoring the

Optical Properties of APCVD Titanium Oxide Films for All-Oxide Multi-Layer Anti-Reflection Coatings," *IEEE Journal of Photovoltaics*, vol. 5, pp. 1265–1270, 2015, doi: 10.1109/JPHOTOV.2015.2437272.

[56] R. S. Bonilla, K. O. Davis, E. J. Schneller, W. V. Schoenfeld, and P. R. Wilshaw, "Effective Antireflection and Surface Passivation of Silicon Using a SiO2/a-TiOx Film Stack," *IEEE Journal of Photovoltaics*, vol. 7, no. 6, pp. 1603–1610, Nov. 2017, doi: 10.1109/JPHOTOV.2017.2753198.

[57] "Simulating Metallization Screen Pattern Trends for Silicon Solar Cell Design," *AZoM.com*, Sep. 30, 2013. https://www.azom.com/article.aspx?ArticleID=10059 (accessed May 20, 2022).

[58] S. Guo, G. Gregory, A. M. Gabor, W. V. Schoenfeld, and K. O. Davis, "Detailed investigation of TLM contact resistance measurements on crystalline silicon solar cells," *Solar Energy*, vol. 151, pp. 163–172, 2017, doi: 10.1016/j.solener.2017.05.015.

[59] G. Gregory *et al.*, "Nondestructive Contact Resistivity Measurements on Solar Cells Using the Circular Transmission Line Method," *IEEE Journal of Photovoltaics*, vol. 9, no. 6, pp. 1800–1805, Nov. 2019, doi: 10.1109/JPHOTOV.2019.2945173.

[60] M. J. Hossain *et al.*, "A Comprehensive Methodology to Evaluate Losses and Process Variations in Silicon Solar Cell Manufacturing," *IEEE Journal of Photovoltaics*, vol. 9, no. 5, pp. 1350–1359, Sep. 2019, doi: 10.1109/JPHOTOV.2019.2926628.

[61] X. Qu *et al.*, "Identification of embedded nanotwins at c-Si/a-Si:H interface limiting the performance of high-efficiency silicon heterojunction solar cells," *Nat Energy*, vol. 6, pp. 194–202, Feb. 2021, doi: 10.1038/s41560-020-00768-4.

[62] F. Feldmann, C. Reichel, R. Müller, and M. Hermle, "The application of poly-Si/SiOx contacts as passivated top/rear contacts in Si solar cells," *Solar Energy Materials and Solar Cells*, vol. 159, pp. 265–271, Jan. 2017, doi: 10.1016/j.solmat.2016.09.015.

[63] W. Liu *et al.*, "Polysilicon Passivating Contacts for Silicon Solar Cells: Interface Passivation and Carrier Transport Mechanism," *ACS Appl. Energy Mater.*, vol. 2, no. 7, pp. 4609–4617, Jul. 2019, doi: 10.1021/acsaem.8b02149.

[64] J. F. Mousumi *et al.*, "Phosphorus-doped polysilicon passivating contacts deposited by atmospheric pressure chemical vapor deposition," *Journal of Physics D: Applied Physics*, vol. 54, no. 38, p. 384003, Jul. 2021, doi: 10.1088/1361-6463/ac0e5c.

[65] H. Kim *et al.*, "Passivation properties of tunnel oxide layer in passivated contact silicon solar cells," *Applied Surface Science*, vol. 409, pp. 140–148, Jul. 2017, doi: 10.1016/j.apsusc.2017.02.195.

[66] Q. Wang, W. Wu, N. Yuan, Y. Li, Y. Zhang, and J. Ding, "Influence of SiOx film thickness on electrical performance and efficiency of TOPCon solar cells," *Solar Energy Materials and Solar Cells*, vol. 208, p. 110423, May 2020, doi: 10.1016/j.solmat.2020.110423.

[67] B. W. H. van de Loo *et al.*, "On the hydrogenation of Poly-Si passivating contacts by Al2O3 and SiN thin films," *Solar Energy Materials and Solar Cells*, vol. 215, p. 110592, Sep. 2020, doi: 10.1016/j.solmat.2020.110592.

[68] J. L. Hernández *et al.*, "High Efficiency Copper Electroplated Heterojunction

Solar Cells and Modules – The Path towards 25% Cell Efficiency," *28th European Photovoltaic Solar Energy Conference and Exhibition; 741-743*, p. 3 pages, 1488 kb, 2013, doi: 10.4229/28THEUPVSEC2013-2AO.2.1.

[69] D. Muñoz *et al.*, "Key Aspects on Development of High Efficiency Heterojunction and IBC-Heterojunction Solar Cells: Towards 22% Efficiency on Industrial Size," *27th European Photovoltaic Solar Energy Conference and Exhibition; 576-579*, p. 4 pages, 6032 kb, 2012, doi: 10.4229/27THEUPVSEC2012-2AO.2.3.

[70] P. Papet *et al.*, "Heterojunction Solar Cells with Electroplated Ni/Cu Front Electrode," *28th European Photovoltaic Solar Energy Conference and Exhibition; 1976-1979*, p. 4 pages, 4135 kb, 2013, doi: 10.4229/28THEUPVSEC2013-2DV.3.51.